RSC Advances

REVIEW

View Article Online
View Journal | View Issue

Spinel materials for high-voltage cathodes in Li-ion batteries

Cite this: *RSC Adv.*, 2014, **4**, 154

D. Liu,[a] W. Zhu,[a] J. Trottier,[a] C. Gagnon,[a] F. Barray,[a] A. Guerfi,[a] A. Mauger,[b] H. Groult,[b] C. M. Julien,[c] J. B. Goodenough[d] and K. Zaghib*[a]

Received 10th October 2013
Accepted 5th November 2013

DOI: 10.1039/c3ra45706k

www.rsc.org/advances

The success of lithium-ion batteries in small-scale applications translates to large-scale applications, with an important impact in the future of the environment by improving energy efficiency and reduction of pollution. In this review, we present the progress that allows lithium-insertion compounds with the spinel structure to become the active cathode element of a new generation of Li-ion batteries, namely the 5 V cathodes, which promise to improve the technologies of energy storage and electric transportation, thereby addressing the replacement of the gasoline engine and the increasing demand for green energy power sources. The compounds considered here include the spinel $LiNi_{0.5}Mn_{1.5}O_4$ and its related Cr-doped structure. Emphasis is placed on the control of physical properties that is needed to guarantee the reliability and the optimum electrochemical performance of these materials as the active cathode element of Li-ion batteries. We also report the structural evolution of the spinel phase in both charge (Li extraction) and discharge (Li insertion) reactions.

Published on 06 Ximoli 2013. Downloaded on 06/02/2026 5:32:02 AM.

A Introduction

Developing cathode materials with high energy densities is one of the key challenges for adopting the lithium-ion battery technology for the hybrid electric vehicle (HEV) and the plug-in hybrid electric vehicle (PHEV) applications. A high energy density can be obtained either by high voltage or high capacity.[1–3] With a high operating voltage around 4.7 V and a practical capacity (about 130 mA h g^{-1}) comparable to that of $LiCoO_2$ (~140 mA h g^{-1}) and $LiFePO_4$ (~160 mA h g^{-1}), spinel $LiNi_{0.5}Mn_{1.5}O_4$ provides a specific energy (~610 W h kg^{-1}) higher than that of many commercialized compounds. Since the demonstration of lithium intercalation–deintercalation reversibility in $LiMn_2O_4$,[4] mixed lithium transition-metal oxides with spinel structure have been considered as possible candidates for cathode materials in lithium ion secondary batteries.[5] The interstitial space of the spinel framework provides 3D channels for high-rate Li^+ conduction. Moreover, the Mn^{4+} of the $LiNi_{0.5}Mn_{1.5}O_4$ spinel, herein after named LNM, lowers both the Ni^{3+}/Ni^{2+} couple to 4.7 V and the top of the O-2p bands to 4.8 V *versus* Li to provide a high voltage cathode that operates on both the Ni^{3+}/Ni^{2+} and Ni^{4+}/Ni^{3+} couples with no significant voltage step between them. Following the early work of Amine *et al.*,[8] LNM and related compounds have attracted considerable attention from many research groups in the field of energy storage; more than 300 papers have been published so far,[6–77] and this number increases rapidly.

Terada *et al.*[15] revealed that the plateau at around 4.7 V is due to the Ni^{2+}/Ni^{4+} redox, whereas a small plateau at 4.1 V arises from the Mn^{3+}/Mn^{4+} redox couple, as observed by *in situ* X-ray absorption fine-structure spectroscopy (XAFS) analysis for the $Li_{1-x}Ni_{0.31}Mn_{1.69}O_4$ material. For the ideal $Li^{+}Ni_{0.5}^{2+}Mn_{1.5}^{4+}O_4$ composition, *i.e.* in the absence of any deviation from stoichiometry, the oxidation state of Mn should be fixed at +4, resulting in only the Ni^{2+}/Ni^{4+} redox couple during the charge–discharge process. The access to two nickel redox couples, Ni^{3+}/Ni^{2+} and Ni^{4+}/Ni^{3+}, at ~4.7 eV below the Fermi energy of a lithium metal anode with a negligible voltage step between the two couples leads to a theoretical gravimetric capacity of 146.7 mA h g^{-1}. At high potential, LNM delivers an energy density equivalent to ~650 W h kg^{-1} of active material. This value is the highest among commercially available cathode materials such as $LiCoO_2$ (518 W h kg^{-1}), $LiMn_2O_4$ (400 W h kg^{-1}), $LiFePO_4$ (495 W h kg^{-1}) and $LiCo_{1/3}Ni_{1/3}Mn_{1/3}O_2$ (576 W h kg^{-1}). Advantages and drawbacks of $LiNi_{0.5}Mn_{1.5}O_4$ have been pointed out: this cathode material includes inexpensive and environmentally benign manganese and it has high electronic and Li^+ ion conductivities, excellent rate capability and good safety, but a severe capacity fade at elevated temperatures (~60 °C) is the main disadvantage.[16]

The first member of the Li–Mn oxide family that has been commercialized is $LiMn_2O_4$, which crystallizes in the spinel structure (S.G. $Fd\bar{3}m$). Li and Mn cations occupy tetrahedral (8a)

[a]*Energy Storage and Conversion, Research Institute of Hydro-Québec, 1800 Bd Lionel-Boulet, Varennes, Québec, J3X 1S1, Canada. E-mail: karim.zaghib@ireq.ca*
[b]*Université Pierre et Marie Curie – Paris6, Institut de Minéralogie et Physique de la Matière Condensée (IMPMC), 4 place Jussieu, 75005 Paris, France*
[c]*Université Pierre et Marie Curie – Paris6, Physicochimie des Electrolytes, Colloïdes et Sciences Analytiques (PECSA), 4 place Jussieu, 75005 Paris, France*
[d]*The University of Texas at Austin, 1 University Station C2220, Austin, USA*

This journal is © The Royal Society of Chemistry 2014

Published on 06 Ximoli 2013. Downloaded on 06/02/2026 5:32:02 AM.

Table 1 Structural parameters of $LiNi_{0.5}Mn_{1.5}O_4$ based on disordered ($Fd\bar{3}m$ S.G.) and ordered ($P4_332$ S.G.) phase

Space group	Atom	Wyckoff position	x	y	z
$Fd\bar{3}m$	Li	8a	1/8	1/8	1/8
	Ni	16d	1/2	1/2	1/2
	Mn	16d	1/2	1/2	1/2
	O	32e	0.263	0.263	0.263
$P4_332$	Li	8c	0.012	0.012	0.012
	Ni	4a	5/8	5/8	5/8
	Mn	12d	1/8	0.3791	−0.1291
	O1	8c	0.3863	0.3863	0.3863
	O2	24e	0.1492	−0.1467	0.1313

and octahedral (16d) sites, respectively, in a cubic close-packed array of oxygen atoms (32e sites). $LiNi_{0.5}Mn_{1.5}O_4$ crystallizes in two possible crystallographic structures: the face-centered spinel (S.G. $Fd\bar{3}m$), called "disordered spinel", and the simple cubic phase (S.G. $P4_332$) called "ordered spinel" (Table 1).[17–19]

The diffraction patterns of the cubic $P4_332$ symmetry is characterized by additional weak Bragg lines located at $2\theta = 15.3$, 39.7, 45.7 and 57.5° due to the 1 : 3 ordering of the Ni and Mn cations.[17,19,20] The cubic cell parameter falls from $a = 8.243$ Å for $LiMn_2O_4$ to $a = 8.1685$ Å for $LiNi_{0.5}Mn_{1.5}O_4$. In the ordered phase, the larger Ni^{2+} ions (ionic radius 0.69 Å) occupy only the 4b sites that give more room than the 16d sites of the normal spinel structure. The cation distribution in the $P4_332$ symmetry is then Li on 8c, Ni on 4b, Mn on 12d, and O(1) and O(2) oxygen ions occupy the 24e and 8c Wyckoff positions, respectively. The net result is thus a significant optimisation of space occupation leading to a reduced unit cell volume. Oxygen loss in the LNM framework leads to Mn^{3+} generated to keep the electric neutrality, and the larger ionic radius of Mn^{3+} (0.645 Å) compared to Mn^{4+} (0.530 Å) results in a larger cell volume (Fig. 1).

The present review gives the state-of-the-art understanding of the properties of LNM and Cr-doped LNM materials. Owing to the evolution in this field, these compounds are promising active 5 V cathode elements for the next generation of Li-ion batteries to improve the technology of the energy storage and electric transportation. This progress is the fruit of about a decade of intensive research in the electrochemical community during which chemists, electrochemists, and physicists have added their efforts to understand the properties of the materials, although some obstacles still stay in the way before 5 V batteries can find their commercial use for worldwide applications in the industry.

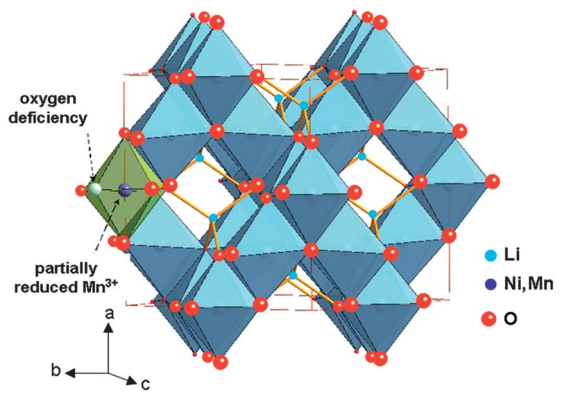

Fig. 1 The structure of spinel $LiNi_{0.5}Mn_{1.5}O_4$ ($Fd\bar{3}m$ S.G.). Oxygen deficiency partially reduces Mn^{4+} to Mn^{3+} to satisfy local charge neutrality.

B Synthesis

Previous studies have shown that the synthesis of single-phase $LiNi_{0.5}Mn_{1.5}O_4$ is a difficult task; this is mainly due to the presence of undesired impurities such as NiO and $Li_xNi_{1-x}O$ in the final product, which deteriorates its electrochemical behaviour.[21–24] Among the various methods used to prepare LNM powders as cathode materials for Li-ion batteries, the most popular are solid state reaction and wet chemical (solution synthetic) method with different morphologies and sizes.

1 Ordered *vs.* disordered LNM

Ordering of the Ni^{2+} and the Mn^{4+} ions on the octahedral sites reduces the deviation from stoichiometry due to oxygen vacancies. The loss of oxygen can introduce a rock-salt impurity phase, *i.e.* $Li_2(NiMn)O_3$, and, as we shall see in Section 5, the appearance of a shoulder at ~4.1 V *vs.* Li^+/Li^0 in the charge and discharge curves, which is indicative of the presence of Mn^{3+} in the spinel phase. The presence of the rock-salt impurity phase with a host spinel phase containing Mn^{3+} is commonly observed after firing at 800–1000 °C.[25] Interestingly, cationic substitutions for Ni have been shown recently to prevent the formation of $Li_xNi_{1-x}O$ impurity and stabilize the spinel structure with a disordering of the Mn^{4+} and Ni^{2+} ions in the 16d octahedral sites. We shall return on this effect in Section 2.5. It also favors the cation disordered structure reflected in a transformation of the space group from $P4_332$ to $Fd\bar{3}m$.[22,26] During the synthesis of the $LiNi_{0.5}Mn_{1.5}O_4$, however, the high calcination temperature sometimes leads to the reduction of the Mn oxidation state from +4 to +3. To cure this oxygen deficiency, some authors employed an annealing process at 700 °C in air after the high-temperature calcination at temperatures as high as 1000 °C, or 500 °C in oxygen atmosphere at high pressure.[27,28] The resulting powders delivered flat voltage profiles at around 4.7 V. Idemoto *et al.*[27] reported that $LiNi_{0.5}Mn_{1.5}O_4$ synthesized under O_2 atmosphere has the cubic spinel structure with a space group of $P4_332$ instead of $Fd\bar{3}m$, as determined by neutron diffraction. Another approach to tune the ordered/disordered phase is an acute control of the cooling rate immediately after high temperature calcinations.[29]

2 Solid state reaction

Generally, the $LiMn_{1.5}Ni_{0.5}O_4$ powders prepared by solid-state reaction (SSR) have a large deficiency in oxygen, which results in the appearance of a wide voltage plateau at 4.1 V *vs.* Li^+/Li and the presence of a rock-salt impurity phase such as NiO or $Li_xNi_{1-x}O$. It is thus detrimental to the electrochemical properties. The amount of impurity phase can be reduced by annealing the sample in high O_2 pressure (at *ca.* 2 MPa).[30] Spinel

Published on 06 Ximoli 2013. Downloaded on 06/02/2026 5:32:02 AM.

oxides were synthesized using carbonates,[31] mixture of Li_2Co_3, NiO and electrolytic MnO_2 as reactants.[32–34] The study of non-stoichiometric $Li_{1\pm x}Ni_{0.5}Mn_{1.5}O_4$ ($x = 0.05, 0$) powders synthesized by SSR revealed that the stoichiometric LNM has the best cycle performance.[33] Modified solid-state reactions include a one-step process,[35] mechanical activated SSR,[36] and ball milling.[37] To obtain pure $LiNi_{0.5}Mn_{1.5}O_4$ powders, the molten salt method was employed with LiCl–LiOH mixed salts.[20]

3 Wet-chemical route

Many approaches have been used to synthesize LNM by wet-chemical methods or "chimie douce" using aqueous or alcoholic solutions providing high-purity spinel phase.[38] These techniques include combustion method,[39] co-precipitation method (CPM),[40] ultrasonic CPM,[41] two-dryness CPM,[42] emulsion drying,[43] oxalate co-precipitation process.[44] The sol–gel method is the most popular technique to prepare spinel phases.[45–47] Choy *et al.*[46] prepared the spinel by a modified citrate route at a pH of 6.4 using Li carbonate and Mn nitrate. Lee *et al.*[47] prepared the spinel from an aqueous solution of acetate salts. Pure $LiNi_{0.5}Mn_{1.5}O_4$ phase was also produced using a chelating agent.[48] Therefore, the material synthesized by the sol–gel method is expected to have enhanced electrochemical performance and has been extensively investigated. Cao and Manthiram proposed a novel synthetic approach using urea as a reservoir for CO_2 to control the formation of LNM and optimize its morphology for high tap density.[49] Various raw materials have also been used, including acetates, hydroxides, nitrates, mixture of precursors,[50] or nitrate and polyvinyl acetate with subsequent decomposition at 150 °C.[30] Idemoto *et al.*[51] have investigated the crystal structure and the electrode performance as a function of sol–gel synthetic conditions. The obtained LNM electrodes fired at 700 °C showed a maximum discharge capacity of *ca.* 125 mA h g^{-1}, and the capacity after 100 cycles was 95.1% of the initial one at low C-rate and at room temperature. Cabana *et al.*[52] prepared by different synthetic routes, *i.e.* mixed hydroxide route and hydrothermal method, a series of LNM samples that displayed a variety of particle sizes and shapes, from nanometric to micrometric, with different anisotropies and assemblies. A modified Pechini method utilized metal nitrates dissolved in distilled water and added drop-wise to citric acid–ethylene glycol (1 : 4 molar ratio); this solution heated to 140 °C enables the chelation (reaction of functional carboxyl group of acid with metal ions) process for the esterification of acid with ethylene glycol. The final product is composed by primary crystallites of 50–70 nm size with a surface area of 15.6 m^2 g^{-1}.[53]

The co-precipitation synthetic route provides good crystallization of the $Fd\bar{3}m$ phase with disordered Ni and Mn.[54] This method is described as follows. Stoichiometric amounts of manganese, lithium, and nickel acetates (99% Aldrich) were first dissolved in distilled water and stirred for 1 h. Oxalic-acid solution was then added dropwise under stirring to obtain a green precipitate. The molar ratio of oxalic acid to metal ions was controlled to be 1 : 1. The precipitate solution was continually stirred for 1 h before being dried at 50 °C overnight with constant stirring. The dried precipitate was preheated at 500 °C for 6 h and then ground for 30 min. The preheated powder was pressed into pellets (20 mm dia. and *ca.* 5 mm thick) and annealed at 900 °C for 24 h in air for better crystal growth. Fig. 2 shows typical SEM and TEM images used to characterize the crystallite size and surface morphology of LNM spinel particles. The samples are not only well crystallized, but the powder particles consist of many small grains, most of the observed grains are >0.2 μm without serious agglomeration after annealing at 900 °C for 24 h in air (Fig. 2a). The grains are well crystallized with sharp corners. Some of the grains are thick disks. However, the TEM images (Fig. 2b and c) indicate a polycrystalline microstructure within the particles with nano-size domains of different orientations, some disordered areas, and bent lattice fringes.

4 Other methods

Other synthesis routes are also commonly used including spray pyrolysis,[55] and derivatives methods such as spray drying,[56] ultrasonic spray,[57] ultrasonic spray pyrolysis,[58] spray pyrolysis associated with internal combustion-type.[59] However, the size of the particles obtained by this technique is the order of a micrometer, while smaller particles can be obtained by other techniques including the wet chemistry reviewed in the previous section. The use of polymers containing oxygen-based functional groups [polyethylene glycol (PEG), poly(methyl methacrylate) (PMMA)] has been studied to synthesize highly crystalline nanometric LNM spinel.[11] In the presence of oxalic acid and polymer followed by heating at 800 °C for a few minutes is sufficient to obtain pseudo-polyhedral particles ranging from 60–80 nm in size.

5 Impurity removal

The synthesis of disordered LNM is often accompanied by oxygen loss at high temperature (>715 °C), which results in non-stoichiometric $LiNi_{0.5}Mn_{1.5}O_{4-\delta}$.[20] We have already mentioned that the oxygen removal in LNM may introduce $Li_2(NiMn)O_3$ and $Li_xNi_{1-x}O$ impurities, while partially reducing Mn^{4+} to Mn^{3+} to satisfy local charge neutrality. To suppress the $Li_xNi_{1-x}O$ impurity phase and improve the electrochemical performance, various cation substitutions have been pursued.[60–63] It was found that equal amounts of Cr^{3+} substitution for Ni^{2+} and Mn^{4+} improves the rate capability especially for $LiNi_{0.45}Mn_{1.45}Cr_{0.1}O_4$, due to the segregation of Ni from the surface to the bulk as indicated by energy-dispersive X-ray (EDX) analyses.[62] However, there are still some Ni-based impurities

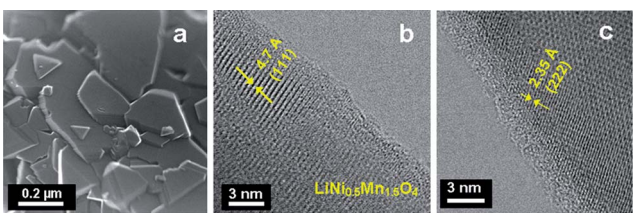

Fig. 2 SEM and TEM images of the LNM particles synthesized by co-precipitation.

 This journal is © The Royal Society of Chemistry 2014

Published on 06 Ximoli 2013. Downloaded on 06/02/2026 5:32:02 AM.

and, as we shall see in Section 5, a small 4.1 V Mn^{3+}/Mn^{4+} redox plateau for the whole series of Cr-substituted LNM. Recently, we used a post-annealing strategy at lower temperature to modify the oxygen deficiency and suppress the Mn^{3+} content while maintaining the disordered structure.[64] With the post-annealing strategy, a pure $LiNi_{0.45}Mn_{1.45}Cr_{0.1}O_4$ disordered phase was successfully synthesized. In the following, we report a comparative analysis of the properties of this Cr-doped LNM, *i.e.* $LiNi_{0.45}Mn_{1.45}Cr_{0.1}O_4$, and a pristine LNM (commercial sample from Energy Innovation Group (EIG), Korea).

C Structural properties

1 X-ray diffraction

Fig. 3a presents the XRD patterns of the spinel samples fired at different temperatures. The peaks at *ca.* $2\theta = 37.7$ and 43.6° are due to the rock-salt impurity phase; their intensity increases with increasing sintering temperature T_s from 700 to 900 °C as a result of the oxygen loss at high temperature. This growth of the impurity phase is correlated with an increase of the lattice parameter by 0.15% between $T_s = 700$ and 900 °C, proof that some oxygen is removed from the host at such temperatures. It is not possible to identify the nature of the impurity, although it is presumably associated with Li_2MnO_3, because its composition varies with T_s, as can be seen in Fig. 3a from the shift of the impurity peak with T_s. Interestingly, the impurity diffraction lines are absent in Cr-doped sample after it was re-annealed at 600 °C, indicating that post annealing is an effective way to eliminate the impurity phase. Moreover, the lattice parameter is increased by 0.34% in the annealing process, so that oxygen is reinserted. On the other hand, it has been reported that the spinel LNM undergoes a thermally induced order/disorder transition at ~700 °C.[65] Therefore, we assume that re-annealing at 600 °C only helps modify the oxygen deficiency while maintaining the disordered structure. In order to characterize the order/disorder of the LNM sample, Rietveld refinement of XRD data was carried out with the Fullprof program in the space group with Li in 8a sites and transition metals statistically distributed in 16d sites. The well-fitted refinement profile given in Fig. 3b for the final sample confirms that the LNM spinel still retains the disordered structure (S.G.). Moreover, Rietveld refinement also gives the cubic lattice parameter $a = 8.16559$ Å, which is close to the value for ordered LNM,[20,66] but different from a previous result of 8.17846 Å.[62] Since the ionic radius of Mn^{4+} is smaller than that of Mn^{3+} and since the increased lattice parameter with the presence of Mn^{3+} results from the oxygen deficiency at high temperature, it is reasonable to conclude that there are fewer Mn^{3+} ions after re-annealing at 600 °C. From the Scherrer's formula:

$$L = 0.9\lambda/B\cos\theta, \quad (1)$$

where λ is the X-ray wavelength and B is the width at an intensity equal to half maximum (FWHM), the coherent length, L, is estimated from the XRD pattern to be $L = 67$ nm.

Note that similar results were obtained for $LiNi_{0.45}Mn_{1.45}Cr_{0.1}O_4$. The same post-annealing strategy at 600 °C as in the case of pristine LNM was used to modify the oxygen deficiency during synthesis of the $LiNi_{0.45}Mn_{1.45}Cr_{0.1}O_4$ cathode for lithium-ion batteries. Structural analyses revealed that post-annealing is an effective way to eliminate the impurity phase without changing the space group. In addition, we found that substitution of Cr^{3+} for Ni^{2+} and Mn^{4+} not only helps to keep the Mn^{4+} oxidation state unchanged ($2Cr^{3+} = Ni^{2+} + Mn^{4+}$), but also introduces greater disorder of the B-site cations in LNM,[62] as we shall see in Section 3.2. This feature will explain why the small amount of Cr substituted for Ni and Mn leads to better rate performance along with cyclability at room temperature, as we shall see in Section 5. The variation with thermal treatment of the particle size and morphology were examined by SEM.[64] Images of the disordered $LiNi_{0.45}Mn_{1.45}Cr_{0.1}O_4$ (Fig. 4) represent the well-crystallized material with a particle size in the range of 0.5–2 μm. The micrographs reveal that the post-annealing at

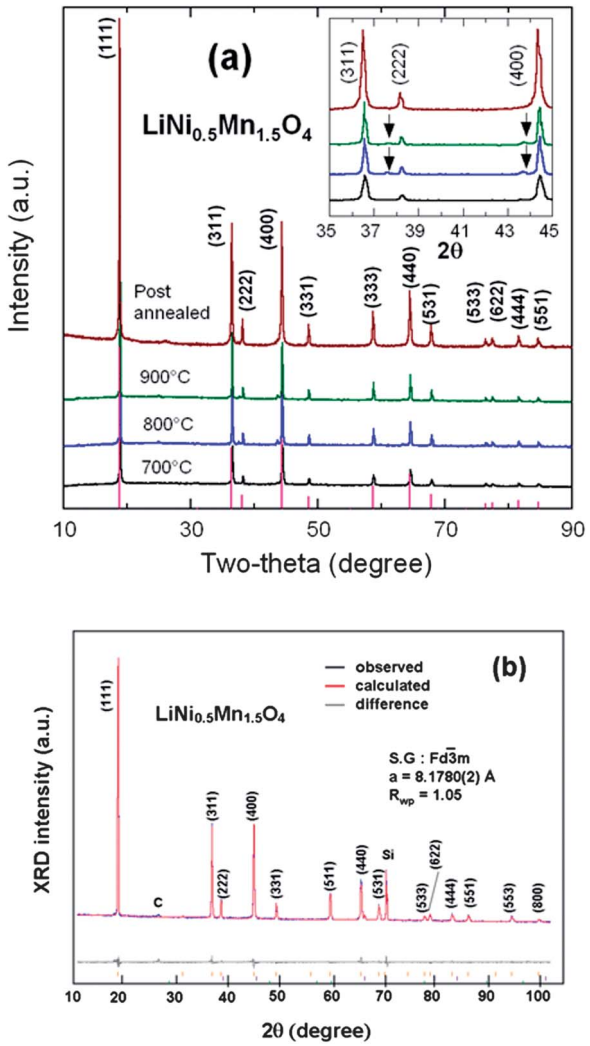

Fig. 3 (a) XRD patterns of the spinel samples at different steps of the synthesis in the temperatures range 700–900 °C before annealing, and for the final sample, post-annealed at 600 °C for 48 h. Inset shows the magnified Bragg lines between $2\theta = 35$–45° with impurity peaks marked by arrows (b) Rietveld refinement profiles of the XRD data for the LNM electrode film (Si peak comes from sample holder). Reproduced with permission.[64]

Published on 06 Ximoli 2013. Downloaded on 06/02/2026 5:32:02 AM.

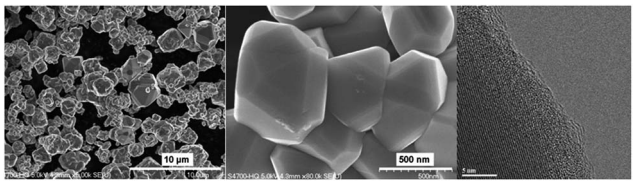

Fig. 4 SEM and TEM images of Cr-doped LNM sample post-annealing at 600 °C.

600 °C promotes well-faced grains of regular shape characteristic of the cubic spinel morphology.

2 Vibrational spectroscopy

FTIR and Raman scattering spectroscopy are powerful techniques to distinguish the order from disorder in LNM,[38,53,65] also used in this work to further investigate the order/disorder change of our samples according to the synthesis parameters. The FTIR spectra of the $LiNi_{0.45}Mn_{1.45}Cr_{0.1}O_4$ sample obtained at different steps of the synthesis are compared in Fig. 5a. The Ni–O stretching vibration at 588 cm^{-1} and the stretching vibration of Mn–O at 619 cm^{-1} dominate the spectra. The characteristic bands (at around 430, 468, 558, and 650 cm^{-1}) corresponding to the cation-ordered structure have a large intensity only in the spectra of the sample fired at 700 °C and are almost absent in the spectra of the other samples, which confirms that the order/disorder transition only occurs at ~700 °C.[20,38,65,67] A semi-quantitative measure of the degree of cation ordering in the spinel sample can be additionally characterized by ratio of the intensity of the main band at 619 cm^{-1} over that of the main additional band present only in the ordered ($P4_332$) phase at 550 cm^{-1}: the larger this ratio, the larger the cation disorder at the molecular range probed by the FTIR technique. Then, the comparison between the FTIR spectrum of the Cr-doped LMN sample and that of the pristine sample post-annealed at 600 °C in Fig. 5a shows that the pristine LNM sample is in a more ordered phase than the Cr-doped sample. Despite the fact that the cations are disordered in the S.G. or O_h^7 spectroscopic symmetry, we find that the FTIR spectrum has well-resolved stretching modes in contrast to the typical spinel $LiMn_2O_4$ exhibiting overlapping broad bands.[38] These vibrational-spectroscopy results can be understood in terms of short-range Ni^{2+}, Mn^{4+} cation ordering on the octahedral sites.

The degree of Ni/Mn ordering in the surface layers of the three samples was also investigated with Raman scattering spectroscopy.[38,54,68] Fig. 5b shows a typical Raman spectrum of crystallized $Li[Ni_{0.5}Mn_{1.5}]O_4$ sample. The octahedral $Mn(Ni)O_6$ structural units have O_h symmetry where the 625 cm^{-1} peak assigned to the symmetric Mn–O stretching vibration of the MnO_6 octahedra in $Li[Mn_2]O_4$ is shifted to 635 cm^{-1}. The new features at 399 ± 1 and 490 ± 2 cm^{-1} are strong and can, therefore, be assigned unequivocally to the Ni–O stretching mode. Two effects contribute to the frequency shift of the Mn–O stretching mode: (a) the increased mean valence state of the Mn ions and (2) a smaller unit-cell volume. None of the peaks characteristic [18] of ordering of the Ni(II) and Mn(IV) in space group $P4_332$ (or $P4_132$), *viz.* at 218, 237 and 607 cm^{-1}, were

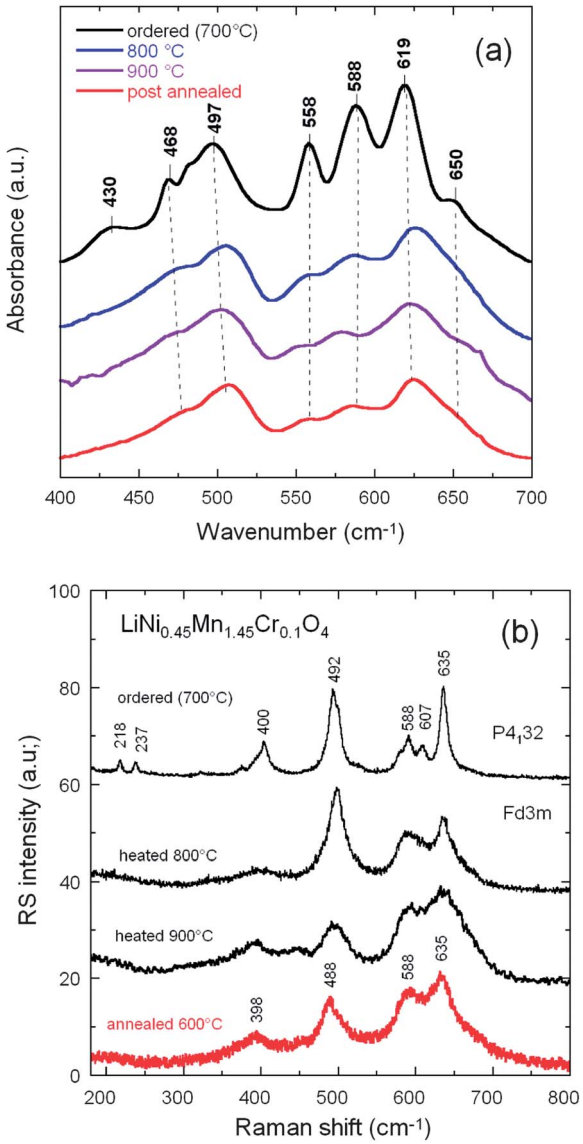

Fig. 5 FTIR (a) and Raman scattering (b) spectra of the $LiNi_{0.45}Mn_{1.45}Cr_{0.1}O_4$ samples obtained at different steps of the synthesis: at different temperatures up to 900 °C before annealing, and for the final sample, post-annealed at 600 °C for 48 h.

detected, which is another indication that the Ni(II) and Mn(IV) of LNM samples were disordered over the 16d sites of the spinel.

Although the vibrational spectroscopy proved very useful to evaluate the degree of cation disorder, it failed to give details on the concentration of oxygen vacancies. In particular, the Mn^{3+}–O stretching mode well observed at circa 518 cm^{-1} in $LiMn_2O_4$ is not detected in our samples. The determination of the concentration of Mn^{3+} ions then requires another means of investigation. We show in the next section that the investigation of magnetic properties fulfils this purpose.

3 Magnetic properties

From now on, we only consider the pristine and Cr-doped samples pot-annealed at 600 °C. Fig. 6a shows the temperature

 This journal is © The Royal Society of Chemistry 2014

Published on 06 Ximoli 2013. Downloaded on 06/02/2026 5:32:02 AM.

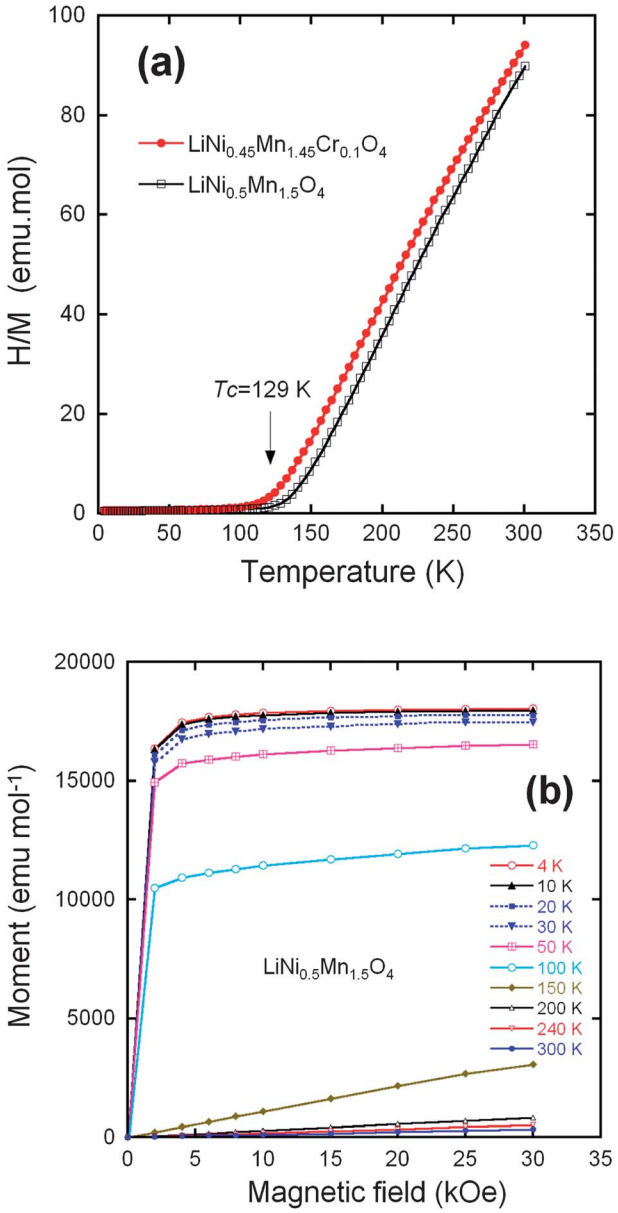

Fig. 6 (a) Inverse of the magnetic susceptibility H/M measured at $H =$ 10 kOe, for the $LiNi_{0.45}Mn_{1.45}Cr_{0.1}O_4$ samples after post annealing at 600 °C and the $LiNi_{0.45}Mn_{1.45}Cr_{0.1}O_4$ crystallized in the same $Fd\bar{3}m$ space group. (b) Magnetization curves of the $LiNi_{0.5}Mn_{1.5}O_4$ sample crystallized in the $Fd\bar{3}m$ space group. Reproduced with permission.[64]

dependence of the reciprocal molar magnetization normalized by magnetic fields (H/M) under an applied field $H = 10$ kOe for the un-doped and Cr-doped $LiNi_{0.5}Mn_{1.5}O_4$ spinel grown by wet-chemical route. The two samples undergo a magnetic transition at a temperature $T_C = 129$ K in LMN, shifted to 117 K in Li $[Ni_{0.45}Mn_{1.45}Cr_{0.1}]O_4$. We argue hereunder that this lowering of T_C is the signature of a reduced amount of short-range order of the Ni^{2+} and Mn^{4+} ions. Fig. 6b displays the field dependence of the magnetization for the Cr-doped spinel at different fixed temperatures. Below 150 K, nonlinearity is clearly observed, suggesting the presence of a strong ferromagnetic contribution. At low temperatures, a typical magnetization curve shows a rapid increase with magnetic field; the magnetic saturation is obtained at a relatively small field. Several authors have reported such a magnetic behavior. Blasse has shown the ferromagnetic spin alignment below 130 K in $LiNi_{0.5}Mn_{1.5}O_4$.[17] Strobel *et al.*[69] found a large increase in the magnetic susceptibility at low temperature, starting at *ca.* 120 K on cooling. These features were attributed to the formation of clusters resulting from a strong magnetic frustration in the structure. Results by Nakamura *et al.*[70] have shown that the asymptotic Curie temperature moved in the positive direction and changed its sign from negative to positive around $y = 0.2$ in $LiNi_yMn_{2-y}O_4$ spinels.

Electron transfer from the half-filled Ni^{2+} σ-bonding e_g orbital to a half-filled Mn^{4+} π-bonding t_g orbital in a 90° Ni^{2+}–O–Mn^{4+} interaction *via* a common $p_{\sigma\pi}$ orbital is restricted by the Pauli exclusion principle to give an antiferromagnetic Ni^{2+}–Mn^{4+} interaction.[71] Ordering of the Ni^{2+} and Mn^{4+} ions in the $P4_332$ $Li[Ni_{0.5}Mn_{1.5}]O_4$ long-range-ordered phase has been shown to give a ferrimagnetic phase at T_C with antiferromagnetic coupling between the Ni^{2+} and Mn^{4+} sublattices.[19] Frustrated magnetic interactions in a completely disordered phase would give a much lower magnetic ordering temperature than in the ordered phase. Therefore, the existence of long-range magnetic order below a T_C similar to that of the ordered $P4_332$ phase is a signature of a strong correlation function $C_{ij} = \langle P(Mn)_i P(Ni)_j \rangle$ with $P(Mn)_i$ $P(Ni)_j$ the probability that if site i is occupied by Mn, site j is occupied by Ni and C_{ij} is large if i and j are nearest 16d-sites. The fact that the peaks of the XRD spectra reported above are well-described in the framework of the disordered phase means that the correlation length C_{ij} is smaller than the length scale probed by XRD, typically a few nm (only an analysis of the diffusive X-ray scattering would give access to the correlation function at shorter length scale). The FTIR in the previous section, which is a probe at the molecular scale, already gave evidence of short-range ordering at this scale. The short-range order is confirmed by the magnetic experiments, which are a probe at the atomic scale and show that the crystal has a large degree of order at the scale of the nearest neighbours.

For long-range order, the saturation magnetization at low temperature results from the difference between the magnetic moment carried by Mn^{4+} and Ni^{2+}. The orbital moment at Mn^{4+} and Ni^{2+} is quenched by the crystal field, which makes a spin-only atomic magnetic moment a good approximation. The spins of Mn^{4+} and Ni^{2+} are $S = 3/2$ and $S = 1$, respectively, so the magnetic moment at saturation for the ordered $LiNi_{0.5}Mn_{1.5}O_4$ should be $(3 \times 1.5 - 2 \times 0.5) = 3.50$ μ_B per formula unit. The experimental value of the saturation magnetization 3.40 μ_B/formula unit at 4.2 K of the phase (Fig. 6b) is in reasonable agreement with the theoretical value for a fully ordered phase and shows the absence of Ni^{3+} ions that would have raised the magnetic momentum to a larger value, as it has been observed in some cases in LNM, ordered or not. The saturation magnetization in the $LiNi_{0.45}Mn_{1.45}Cr_{0.1}O_4$ sample is only reduced to 3.2 μ_B per formula unit. This result suggests that the Cr^{3+} are not distributed randomly, but tend to form antiferromagnetically coupled dimers randomly distributed in the lattice. This is actually expected and implicit in the notation $2Cr^{3+} = Ni^{2+} +$

Published on 06 Ximoli 2013. Downloaded on 06/02/2026 5:32:02 AM.

Mn^{4+}. Two Cr^{3+} on nearest 16d sites form the most favourable configuration to lower the energy for two reasons: first, $2Cr^{3+}$ insures charge neutrality at the molecular scale when substituting for Ni^{2+} + Mn^{4+}, thus minimizing the cost in Coulomb energy; second, the ionic radii r satisfy approximately the relation $2r(Cr^{3+}) \approx r(Mn^{4+}) + r(Ni^{2+})$, so that this substitution also minimizes the lattice distortion. The concentration of Cr is only 5% of the metal ions, *i.e.* far smaller than the percolation threshold of the 16d-site sublattice, and thus too small to destroy the long-range ferrimagnetic ordering at finite temperature; it is, however, responsible for a decrease in the short-range Mn^{4+}, Ni^{2+} order and, therefore of the Néel temperature by 12 K that is observed with respect to $LiMn_{1.5}Ni_{0.5}O_4$. In addition, if we subtract the magnetic moment carried by the Cr^{3+}, 0.3 μ_B per formula, from the Mn and Ni contribution to the magnetic moment at saturation in the antiferromagnetic phase of $LiNi_{0.45}Mn_{1.45}Cr_{0.1}O_4$, we find $1.45 \times 3 - 0.45 \times 2 - 0.3 = 3.15$ μ_B in agreement with the experimental value 3.2 μ_B.

D Electronic properties

1 Density of states and fermi energies

The open-circuit energy diagram of a lithium battery has been discussed by Goodenough *et al.*[1] If the active transition-metal cation contains a localized d-electron manifold, the manifold acts as a redox couple, *e.g.* $Ni^{2+/4+}$ in $LiNi_{0.5}Mn_{1.5}O_4$ spinel. Successive redox couples are separated by an on-site energy U, and the effective U is larger when augmented by either a crystal-field splitting or an intra-atomic exchange splitting.[1] However, when the Fermi energy E_{FC} of the cathode approaches the top of the anion p bands of the host, p–d covalent mixing may transform the d electrons at the E_{FC} into band electrons occupying one-electron states. In the absence of a crystal-field splitting of the d orbitals at E_{FC}, as occurs for Ni(IV) to Ni(II), the one-electron states are not separated by an on-site energy U and there is no step in the voltage of the battery as E_{FC} is moved from one formal valence state to another one upon the reduction or oxidation of the host. The voltage *vs.* lithium that can be obtained with a solid cathode host is constrained by either the intrinsic limit of the cathode host or by the decomposition voltage of the electrolyte if not by the voltage of the electrolyte's highest occupied molecular orbital (HOMO). The intrinsic limit of a host transition-metal compound is the voltage at which E_{FC} becomes "pinned" at the top of the anion p bands.[1]

Fig. 7 reports the schematic density of states and Fermi energies for the $Li_xNi_{0.5-y}Mn_{1.5-y}Cr_{2y}O_4$ spinel cathode. In this case, it may be possible to access two formal valences on the active cation without a voltage step on passing from one formal valence state to the next. However, when E_{FC} of the host falls below the HOMO of the electrolyte, a passivating, Li permeable SEI layer must form on the surface of the active particle if a reversible reaction is to be obtained. If the passivating SEI layer is not permeable to Li^+ ions, it blocks insertion/extraction into/from the host. The HOMO of a liquid carbonate electrolyte is about 4.3 eV below the Fermi energy E_{FA} of a lithium anode, and the decomposition voltage of the electrolyte is at about 5 eV below it. Access to Ni(III) and Ni(IV) valence states is possible in cation disordered $LiNi_{0.5}Mn_{1.5}O_4$ spinel; the SEI layer formed at voltage V >4.3 V is self-limiting and Li-permeable.

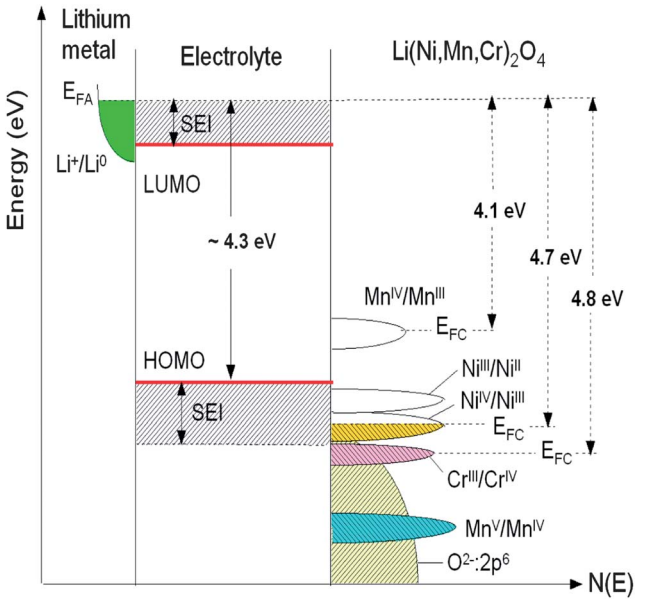

Fig. 7 Schematic density of states and Fermi energies for $Li_xNi_{0.5-y}Mn_{1.5-y}Cr_{2y}O_4$ spinel cathode. The Li permeable SEI layer formed on the electrode surface preserves the overall reversible reaction.

2 Typical voltage profile

Fig. 8 shows the typical voltage profile upon charging a Li//Cr-doped LNM cell recorded at a low rate of C/5. According to the previous considerations, one observes the various redox reactions $Mn^{3+/4+}$ (at 4.1 V), $Ni^{2+/4+}$ (at 4.7 V) and $Cr^{3+/4+}$ (at 4.8 V). The characteristic 4.1 V plateau is always observed in the pristine or metal-doped LNM cathodes as a result of oxygen loss at high-temperature synthesis.[61–63] However, no obvious 4.1 V step

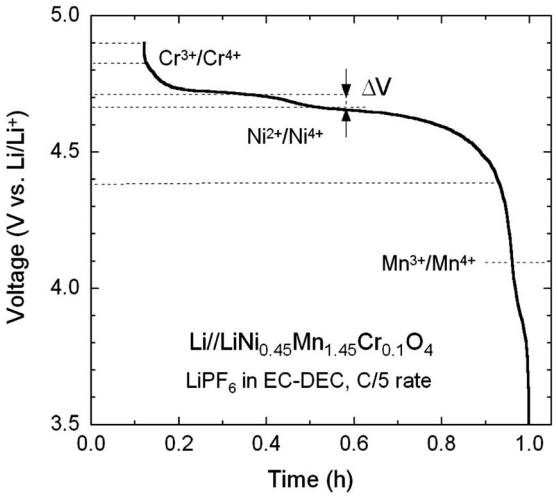

Fig. 8 Typical voltage profile of charge of a Li//Cr-doped LNM cell showing the various redox reactions $Mn^{3+/4+}$ (at 4.1 V), $Ni^{2+/4+}$ (at 4.7 V) and $Cr^{3+/4+}$ (at 4.8 V).

This journal is © The Royal Society of Chemistry 2014

Published on 06 Ximoli 2013. Downloaded on 06/02/2026 5:32:02 AM.

was detected in Cr-doped spinel post-annealed at 600 °C, confirming that most of the residual Mn^{3+} ions have been re-oxidized to Mn^{4+} after heat treatment in agreement with the analysis of magnetic properties. The narrower voltage separation, ΔV, between the two plateaus corresponding to the oxidation peaks of $Ni^{2+/4+}$ in the LNM spinel is indicative the degree of cation ordering on the octahedral 16d sites. The value $\Delta V = \sim 40$ mV for the pristine LNM compared to those $\Delta V = \sim 70$ mV of the Cr-doped LNM is reminiscent of the higher degree of cation ordering in this cathode.

3 Spin configuration

The electrochemical reaction in $Li_xNi_yMn_{2-y}O_4$ has been described by studying the top of the valence band of $LiNi_yMn_{2-y}O_4$ for a series of samples with $0.0 < y < 0.5$.[7] A partial density of states attributed to Ni 3d electrons is located about 0.5 eV above that of the Mn 3d e_g electrons. When $y = 0$, the voltage plateau of $Li//LiMn_2O_4$ is located at 4.1 V. As y increases, the capacity associated to the 4.1 V plateau decreases as $1 - 2y$ Li per formula unit and a new plateau at 4.7 V appears. The capacity associated to the 4.7 V plateau increases as $2y$ Li per formula unit, so that the total capacity of the samples (the sum of the contributions from the 4.1 and 4.7 V plateaus) is constant. This is taken as evidence that the oxidation state of Ni in these samples is +2, and therefore they can be written as $Li^+Ni_y^{2+}Mn_{1-2y}^{3+}Mn_{1+y}^{4+}O_4^{2-}$. The 4.1 V plateau is related to the oxidation of Mn^{3+} to Mn^{4+} and the 4.7 V plateau to the oxidation of Ni^{2+} to Ni^{4+}. The reason for this behaviour could be given by considering the positions of the energy levels shown in Fig. 9. The crystal field splits the 3d levels of Mn and Ni octahedrally coordinated with oxygen into e_g and t_{2g} levels.[7] For Mn^{3+}, among the four $3d^4$ electrons with majority spin (↑) three electrons are on $t_{2g}(\uparrow)$ and one electron is on $e_g(\uparrow)$. The $3d^8$ electrons of Ni^{2+} have six electrons on the $t_{2g}(\uparrow\downarrow)$ levels and two electrons on the $e_g(\uparrow)$ level. When an electron is removed from Mn^{3+}, it is removed from the Mn $e_g(\uparrow)$ state that has an electron binding energy at around 1.5–1.6 eV, and this is on the 4.1 V plateau. When there are no more electrons left on Mn $e_g(\uparrow)$ (all Mn are oxidized to Mn^{4+}), then electrons are removed from Ni $e_g(\uparrow)$ that has an electron binding energy of about 2.1 eV, and the voltage plateau moves up to 4.7 V because of the increased energy needed to remove electrons.

In the case of Cr-doped spinel, the last step of the charge, after all the Mn have been oxidized to Mn^{4+} and Ni to Ni^{4+}, proceeds with the oxidation of Cr^{3+} ions at an upper voltage plateau according to the reaction:

$$Li^+Ni^{4+}_{0.5-y}Mn^{4+}_{1.5-y}Cr^{3+}_{2y}O_4 \rightarrow Ni^{4+}_{0.5-y}Mn^{4+}_{1.5-y}Cr^{4+}_{2y}O_4 + xLi^+ + xe^- \quad (2)$$

Fig. 9 shows the change in the occupation of the energy levels in $Li_xNi_{0.5-y}Mn_{1.5-y}Cr_{2y}O_4$ spinel during the charge process ($x \approx 0.08$) according to this model. Considering the electronic states, the energy difference $\Delta E = 0.5$ eV between the Mn e_g level and the Cr t_{2g} level corresponds to the potential difference between the two plateaus of the discharge profile for the $Li//LiMn_{2-y}Cr_yO_4$ cell (see Fig. 10).

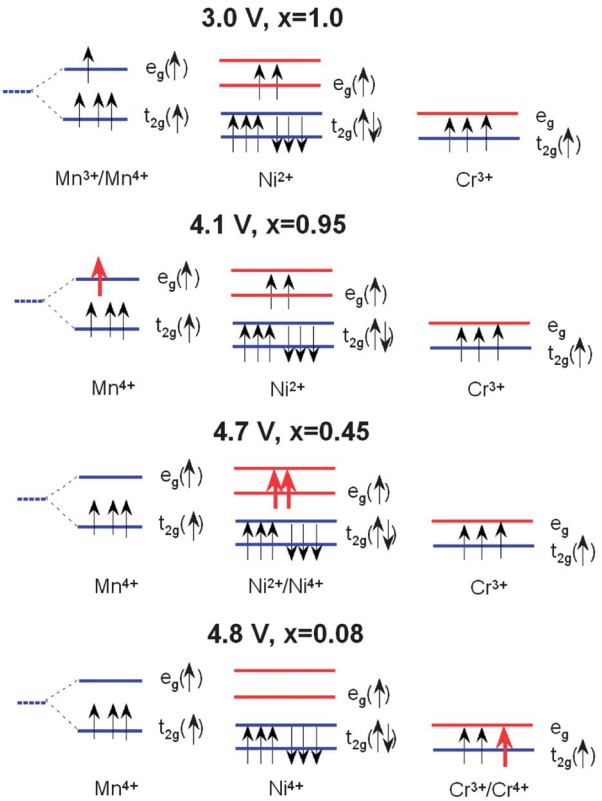

Fig. 9 Schematic diagram showing the 3d electronic levels of Mn^{3+}, Ni^{2+} and Cr^{3+} in $LiNi_{0.5-y}Mn_{1.5-y}Cr_{2y}O_4$ spinel during the charge process. It is noted that Ni^{2+} favours the low-spin configuration in $LiNi_{0.5-y}Mn_{1.5-y}Cr_{2y}O_4$. Partially empty levels are shown with red arrows.

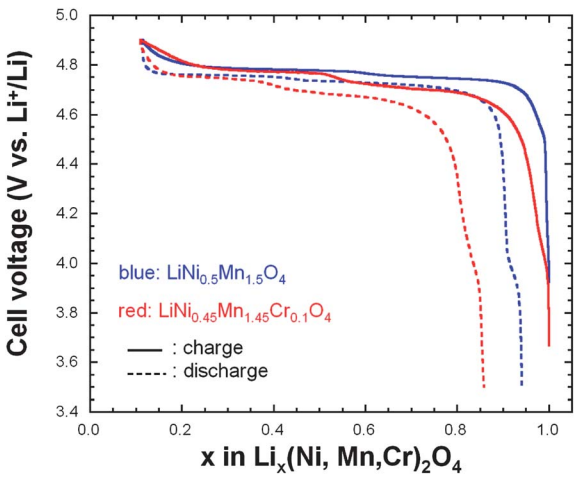

Fig. 10 Charge–discharge curves of the un-doped and Cr-doped LNM cathodes in CR2032 coin cell composed of $LiPF_6$ in EC–DEC (1 : 1) as electrolyte. The cathode electrode contained 89 wt% active material, 6 wt% conductive carbon, and 5 wt% PVdF binder (loading 5 mg cm^{-2}). All cells were cycled at 25 °C between 3.5 and 4.9 V at C/5 rate.

E Electrochemical performance

The electrochemical properties of the un-doped and Cr-doped spinel cathodes were investigated in CR2032 coin cells

Published on 06 Ximoli 2013. Downloaded on 06/02/2026 5:32:02 AM.

composed of $LiPF_6$ in 1 : 1 ethylene carbonate–diethylene carbonate (EC–DEC) as electrolyte. Fig. 10 shows the initial charge–discharge cycle at a low rate of C/5 for both cathode materials. The characteristic 4.1 V Mn^{3+}/Mn^{4+} redox couple is always observed in the pristine or metal-doped LNM cathodes before post-annealing as a result of oxygen loss at high-temperature synthesis.[61–63]

However, in Fig. 10 obtained for the samples post-annealed at 600 °C, no obvious 4.1 V step is detected in $LiNi_{0.45}Mn_{1.45}Cr_{0.1}O_4$ spinel (red curves), confirming that most of the residual Mn^{3+} ions have been re-oxidized to Mn^{4+} after re-annealing at 600 °C in agreement with the analysis of magnetic properties. This is also consistent with the Rietveld refinement of the XRD spectra. However, a small anomaly near 4.1 V can be detected on the discharge curves, pronounced in the case of the un-doped LNM, which suggests that Cr-doping can reduce, but not avoid entirely a loss of oxygen with time during cycling. We shall return to this problem in Section 7. In addition, $LiNi_{0.45}Mn_{1.45}Cr_{0.1}O_4$ shows two distinct plateaus at around 4.7 V. In contrast, the un-doped sample only exhibits a single flat voltage profile at about 4.7 V. No obvious great change was found after 100 cycles, suggesting good reversibility for both samples.

In order to understand the difference in the electrochemical properties of the $LiNi_{0.5}Mn_{1.5}O_4$ and $LiNi_{0.45}Mn_{1.45}Cr_{0.1}O_4$ spinel cathodes, Fig. 11 compares the incremental capacity dQ/dV *vs.* V graphs, where $Q = \int I dt$ from $t = 0$ at 3.5 V to t at V–3.5 calculated from curves in Fig. 10. Removal of Li from the tetrahedral sites of the spinel LNM framework initially probes the oxidation reaction of $Ni^{2+} \rightarrow Ni^{3+}$ just below 4.7 V (typically ~4.69 V) for the disordered $Fd\bar{3}m$ and above 4.7 V (typically ~4.72 V) for the ordered $P4_332$ spinels.[68] Ordering of the Ni and Mn raises by ~0.02 eV the $V(x)$ profile of LNM. From Fig. 11a, two anodic peaks at 4.663 and 4.731 V plus two cathodic peaks at 4.638 and 4.704 V were observed for the $LiNi_{0.45}Mn_{1.45}Cr_{0.1}O_4$, which is in agreement with two voltage plateaus for disordered LNM.[20,68] Kim *et al.* suggested that, as the crystallographic structure changed from $Fd\bar{3}m$ to $P4_332$, the voltage gaps between the two plateaus became narrower at around 4.75 V and resulted in a flatter voltage profile.[67] This separation is known to decrease from about 60 mV to around 20 mV, depending on the degree of ordering.[66–68] The average potential difference, ΔV, between these two peaks is *ca.* 60 mV for the Cr-doped LNM material and 30 mV for the commercial sample. Therefore these results corroborate the much stronger cation disorder induced by the Cr-doping. Additionally, small redox peaks were observed in the $LiMn_{1.45}Cr_{0.1}Ni_{0.45}O_4$ at about 4.85 V, showing the redox reaction between Cr^{3+} and Cr^{4+} and confirming the electrochemical activity of Cr in the Cr-substituted LNM.

The smaller ΔV in un-doped LNM compared to that of $LiNi_{0.45}Mn_{1.45}Cr_{0.1}O_4$ suggests faster lithium insertion/extraction kinetics in the former.[72] This is, however, controversial because it is well known that the cation disorder and the decrease of the concentration of defects such as oxygen vacancies is beneficial to the electrochemical performance. Therefore, the $LiNi_{0.45}Mn_{1.45}Cr_{0.1}O_4$ should have the best properties, and actually, this was the

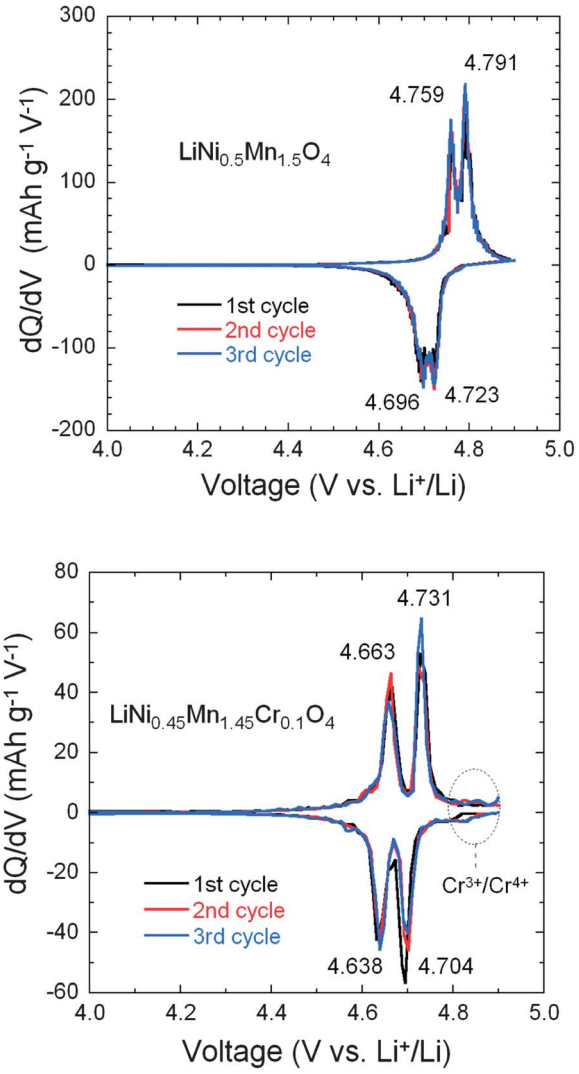

Fig. 11 Differential capacity curves, dQ/dV *vs.* V, of the un-doped LNM (top) and $LiNi_{0.45}Mn_{1.45}Cr_{0.1}O_4$ (bottom). The values at the peaks are given in volt. Reproduced with permission.[64]

motivation for Cr-doping. Some insight into the insertion/extraction of Li is provided by the modified Peukert plot in Fig. 12 for both un-doped and Cr-doped LNM cathodes. The capacity loss after 25 cycles at 5 C rate is 32.4% and 16.3%, respectively. It is necessary to note that only 6% of conductive carbon was used to make the cathode electrode in this work.

From Fig. 12, the $LiNi_{0.45}Mn_{1.45}Cr_{0.1}O_4$ exhibits better rate capability and capacity retention than $LiNi_{0.5}Mn_{1.5}O_4$. For instance, the $LiNi_{0.45}Mn_{1.45}Cr_{0.1}O_4$ delivered a reversible capacity of ~115, 104, 95 and 40 mA h g^{-1} at C/5, 1 C, 2 C and 5 C, respectively; the un-doped LNM offered a lower reversible capacity of ~110, 98, 85 and 12 mA h g^{-1} at the same C rates. When returned to C/5 from 5 C after 100 cycles, about 99% of reversible capacity was retained for $LiMn_{1.45}Cr_{0.1}Ni_{0.45}O_4$ *vs.* 94% for un-doped LNM. These results give evidence that the electrochemical properties of the Cr-doped sample are definitely better than those of the un-doped sample at high C-rate, as expected. Therefore, the lower value of ΔV in un-doped LNM

This journal is © The Royal Society of Chemistry 2014

Published on 06 Ximoli 2013. Downloaded on 06/02/2026 5:32:02 AM.

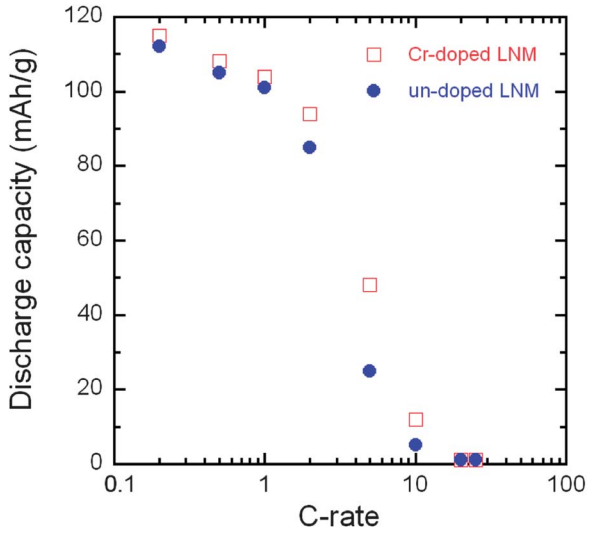

Fig. 12 Modified Peukert curves of LNM and $LiNi_{0.45}Mn_{1.45}Cr_{0.1}O_4$ spinel cathodes cycled between 3.5 and 4.9 V in CR2032 coin cell with $LiPF_6$ in EC–DEC (1 : 1) as electrolyte.

cannot be attributed to lower kinetics in the Cr-doped sample. To understand this difference in ΔV between the two samples, the phase diagram must be investigated; this is the purpose of the next section.

F Phase diagram

The phase evolution during lithium de-intercalation/intercalation within these two spinels has been studied using both *ex situ*,[67,73] and *in situ* X-ray diffraction techniques.[53,74–77] Conflicting results have been reported. In the ordered LNM, three distinct cubic phases were detected relating to each of the Ni^{2+}, Ni^{3+}, and Ni^{4+} oxidation states in the ordered LNM material. These phases transformed from one to another by means of two distinct two-phase regions that correspond to the wide voltage plateaus observed in the electrochemical profile of the cathodes.[20,53] In contrast, the disordered LNM material showed a smooth peak shift to higher angles with no clear two-phase region until nearing the end of charging, which is observed by less pronounced plateaus in the voltage profiles.[20,53] On the other hand, a structural change has been reported upon delithiation of disordered $Li_xNi_{0.5}Mn_{1.5}O_4$ at $x = 0.5$ with loss of the glide symmetry.[67] However, a different phase diagram has been reported for this same disordered LNM, with a solid solution for large values of x, followed with a two-phase region at $x \sim 0.6$, with the onset of a second cubic phase, phase II, and another two-phase region at $x < 0.4$, where phase II coexists with another cubic phase, phase III.[74] Rhodes *et al.*[75] found the three phases co-existing in a finite range of concentrations. However, the authors did not specify if their measurements were made on ordered or disordered LNM. We can simply note that their result is in agreement with the phase diagram found for LNM in the ordered phase, since the three phases are found to co-exist only in this case.[74] Moreover, the phase diagram is reported to depend on the morphology of the particles.[76]

Since the disordered LNM outperforms the ordered LNM as a cathode element for Li-ion batteries, we found it desirable to clarify the phase diagram of LNM in the disordered phase. The purpose of this work is to report the study of the structural changes of LNM during lithium extraction and insertion by *in situ* XRD measurements. Since, in addition, oxygen vacancies have undesirable effects mentioned above; this investigation has been made both on un-doped and Cr-doped LNM that is free of oxygen vacancy.[64,77] The differences in phase evolution were compared and the effect of Cr substitution is discussed.[77]

The evolution of *in situ* XRD patterns of the Cr-doped LNM electrode during the cycling at C/24 rate is reported in Fig. 13, in which (311) and (511) Bragg lines have been selected to understand better the phase evolution. Overall, all the diffraction peaks shifted to the higher 2θ angles as the Li^+ ions were removed from the two host structure. The analysis of the XRD pattern shows that all the phases are cubic, and the lattice parameters for each phase as a function of x over one charge–discharge cycle are reported in Fig. 14.

As charge proceeds from $x = 1$, a solid solution is observed in the whole range $1 \leq x \leq 0.72$, the decrease in Li resulting only in the decrease of the lattice parameter of the cubic phase that we label as phase-1. A new cubic spinel phase (phase-2) started to emerge and the system thus undergoes a first-order transition at $x = 0.72$, to enter in a two-phase domain $0.72 \leq x \leq 0.54$, in which the phase-2 grows at the expense of the phase-1, so that the phase-1 disappears at the Li concentration $x = 0.54$. Below this concentration, we find a small but finite range of concentration $0.54 \leq x \leq 0.37$, in which the Cr-doped is again a solid

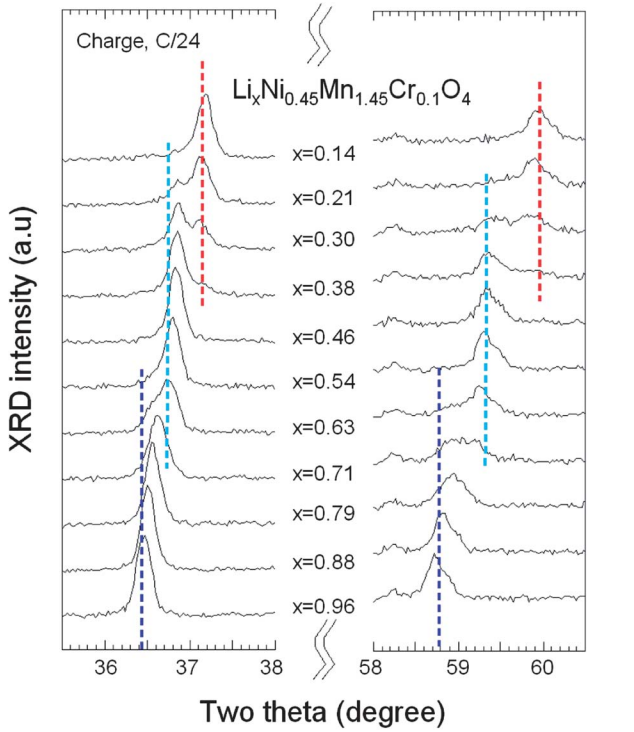

Fig. 13 *In situ* XRD patterns of the (311) and (511) peaks as a function of x(Li) of Cr-doped LNM spinel during the charge at C/24 rate.

Published on 06 Ximoli 2013. Downloaded on 06/02/2026 5:32:02 AM.

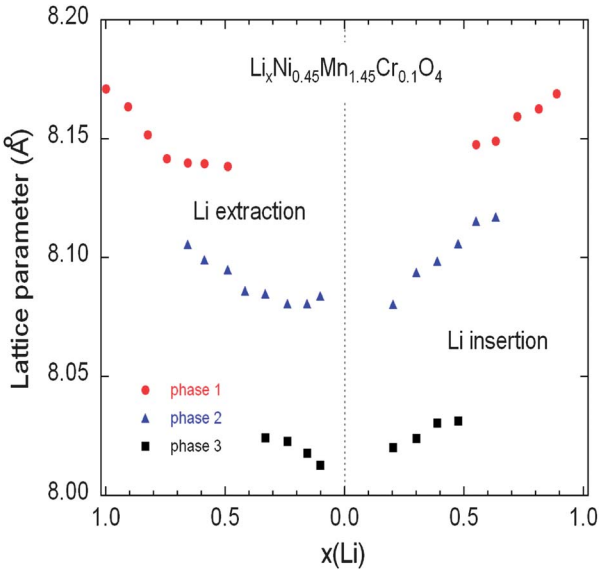

Fig. 14 Variation of the lattice parameters of the different cubic phases in the Cr-doped LNM sample as a function of the Li concentration x during the charge (a) and discharge (b) during cycling at C/24 rate. Reproduced with permission.[77]

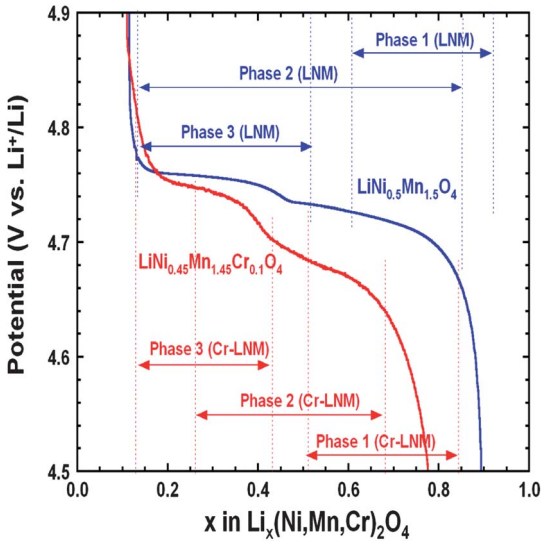

Fig. 15 Variation of the voltage as a function of the Li concentration x in un-doped and Cr-doped LNM samples during discharge of cells cycled at C/24 rate in relation to the phase diagram. Reproduced with permission.[77]

solution in the phase-2 only. The system re-enters a two-phase region in the range $0.37 \leq x \leq 0.13$ with the coexistence of phase-2 and a new phase (phase-3) that grows at the expense of phase-2. Finally, a solid solution with phase-3 only is observed in the range $x \leq 0.13$. The experimental XRD spectra have been measured along the cycle with steps $\Delta x \sim 0.1$, so that the uncertainty in the estimates of the Li-concentrations of the phase boundaries can be estimated to ± 0.05. Upon discharge, phase-3 is found to be a solid solution up to $x = 0.25$. This result gives evidence that, even at the low C-rate of the experiment, thermodynamic equilibrium at the end of the charge was not reached. At the end of charge a very small faction (few% only) of phase-2 is still detectable. However, during the period of time the sample has been let in open-circuit before the cell was discharged, this phase-2 has been converted into phase-3 only. This can also be seen as the discontinuity between the end of discharge and the beginning of charge. Therefore, at equilibrium, the Cr-doped sample will be in a solid solution in phase-3 at low values of $x \leq 0.25$. Upon discharging, the phase-2/phase-3 system is found in the range $0.26 \leq x \leq 0.43$. The difference between 0.37 and 0.43 does not exceed the experimental uncertainty and is thus negligible. The onset of phase-1 in phase-2 is also the same at charge and discharge. Therefore, within this experimental uncertainty, we can deduce that the phase transformations are totally reversible, without any hysteresis, except for a small shift concerning the limit in the solid solution in phase-3 that, however, is not an intrinsic effect; it is clearly an artefact due to deviation from equilibrium.

To understand the link between the phase diagrams determined in the previous section and the electrochemical properties. We have reported in Fig. 15 the variation of the voltage with x for the two samples together with the range of existence of the different phases. First, we observe that the voltage of the battery with the Cr-doped sample is smaller than with the un-doped sample at any Li concentration x, except in the small region $0.1 \leq x \leq 0.2$. The unexpected larger value of the voltage in this small region is clearly attributable to the fact that a larger proportion of phase-2 is still observed in the un-doped LNM sample in this range of concentration. Since the voltage associated to the phase-2 is lower than that of phase-3, the persistence of this phase lowers the potential, which becomes lower than in the Cr-doped sample where only the phase-3 is observed. Second, we also note that the voltage is strongly dependent of the composition in this small range of composition. This is true for the case of the Cr-doped sample, and this is expected since the Cr-doped sample is a solid solution in phase-3. In case of a two-phase regime, however, the Gibbs rule tells us that $V(x)$ should be a flat plateau, while the potential varies very fast with x in this region. Therefore, the strong variation of $V(x)$ in the un-doped sample in the small range $0.1 \leq x \leq 0.2$ confirms that it is not in a two-phase regime. Instead, it should be considered as a solid solution in phase-3. The presence of the phase-2 simply means the existence of some isolated phase-2 clusters attributable to the difficulty to reach thermodynamic equilibrium.

G Surface modification

Despite the interesting electrochemical properties of LNM, two problems need be solved before the material may conquest the market and find a commercial development. One is the loss of oxygen. Indeed, the pressure of oxygen at thermodynamic equilibrium in all the oxides of transition metals increase linearly with the potential, favoring the loss of oxygen that causes thermal runaway and battery fires.[78] The other problem comes from the proximity between the Fermi energy and the highest occupied molecular orbital (HOMO) of the carbonate electrolyte, so that a passivating solid/electrolyte-interface (SEI) layer is formed to

 This journal is © The Royal Society of Chemistry 2014

Published on 06 Ximoli 2013. Downloaded on 06/02/2026 5:32:02 AM.

obtain the reversible Ni(IV)/Ni(II) redox reaction.[1] The surface reactions between cathode/electrolyte have been confirmed to be one of the major reasons leading to the degradation in the electrochemical performance of the 4.7 V spinel.[79] Moreover, the chemical reactions with the electrolyte increase with temperature. The consequence is the important capacity fade,[16] at ~60 °C, as already noticed in the introduction, which disqualifies this battery for use in hybrid or electric vehicles. To overcome these problems, various metal oxides, carbon and phosphates[80–85] have been used as surface coatings to improve the electrochemical performance of the LNM particles.

More recently, we have successfully used $LiFePO_4$ as a coating of LNM particles.[86] This process allowed us to take benefit from the fact that $LiFePO_4$ (LFP) shows very good rate performance not only at room temperature but also at 60 °C.[87,88] In addition, in contrast with the transition metal oxides, the oxygen forms covalent bonding with P, to form PO_4 phosphate units that are very stable, so that LFP shows an excellent thermal stability and is also stable in the battery up to a high voltage of 5.4 V. As usual with LFP, its low electrical conductivity implies that is must be carbon coated, so that the particles are multi composite, with a LNM core surrounded by a LFP coat, with conductive carbon on top of it.[86] Fig. 16 shows the modified Peukert plot before and after C–LFP coating. The performance at high C-rate is improved importantly in the multi-composite. This is confirmed in Fig. 17 showing a major improvement induced by the C–LFP coat on the aging of the cell upon cycling. Therefore, the C–LFP coating is a promising technology to protect the LNM particles against the reaction with the electrolyte and to prevent the oxygen loss.

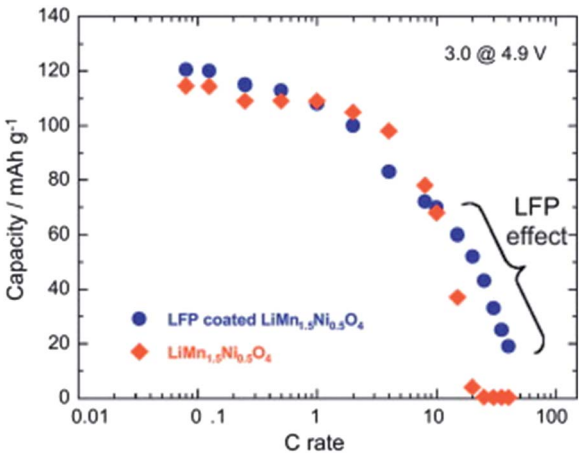

Fig. 16 Modified Peukert plot for the Li//LMN and Li//LFP-coated LMN cells between 3.0 and 4.9 V *vs.* Li^+/Li^0.

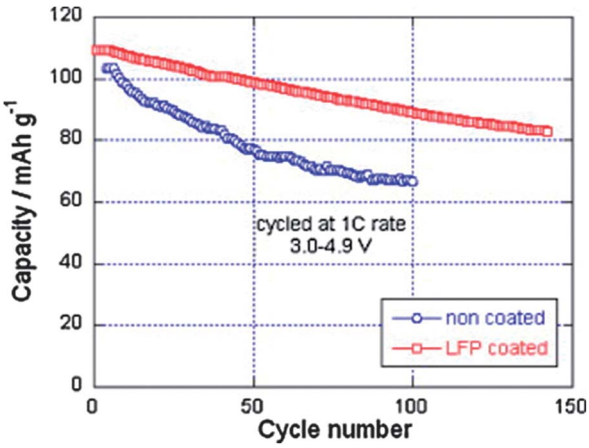

Fig. 17 Cyclability of the Li//LMN and Li//LFP-coated LMN cells at 1 C between 3.0 and 4.9 V *vs.* Li^+/Li^0. Reproduced with permission.[86]

H Conclusions

The rate capability of lithium extraction/insertion is better in the disordered LNM (S.G. $Fd\bar{3}m$) phase because the electronic conductivity in this phase is several orders of magnitude larger than in the ordered phase, and because the diffusivity of lithium ions is higher. The larger electronic conductivity was attributed to the presence of oxygen vacancies in the disordered phase, but it is more likely an intrinsic property. In the stoichiometric composition of $LiNi_{0.45}Mn_{1.45}Cr_{0.1}O_4$, the cations exist as Ni^{2+} and Mn^{4+}, so that they do not carry the same electronic charge. Therefore, the ordering between Mn and Ni is also a charge ordering that will result in the opening of an electrostatic gap.

The structural evolution of un-doped and Cr-doped LNM spinels in the $Fd\bar{3}m$ phase as a function of the Li content (x) investigated by *in situ* XRD analyses shows that both charge (Li extraction) and discharge (Li insertion) reactions occur with the existence of three phases that form alternatively solid solutions and two-phase regions. The results have been understood on the basis of a model[77] that takes strain effects into account, also explaining the fact that the phase diagram is sample dependent, differs between the different results reported in the literature. The analysis of the phase diagram confirms the faster dynamics of the Li-insertion/de-insertion in the Cr-doped sample, evidenced by the improved capacity retention at high C-rates. The other benefit of the Cr-substitution is the increase of the stability of the lattice. The drawback is a decrease in the energy density that is not due to a loss of capacity, but a smaller redox potential of the nickel *vs.* Li^+/Li. Although the coating of the particles with C–$LiFePO_4$ efficiently protects LNM against the surface reactions with the electrolyte, which was the main limiting factor for this material, making LNM the most promising material to obtain high-voltage Li-ion batteries.

References

1 J. B. Goodenough and Y. Kim, *Chem. Mater.*, 2010, **22**, 587.
2 S. Sawa, S. Okada and A. Yoshino, *J. Power Sources*, 2001, **97–98**, 430.
3 R. Ruffo, R. A. Huggins, C. M. Mari, M. Piana and W. Weppner, *Ionics*, 2005, **11**, 213.
4 M. M. Thackeray, P. J. Johnson, L. A. De Picciotto, P. G. Bruce and J. B. Goodenough, *Mater. Res. Bull.*, 1983, **18**, 461.
5 J. W. Fergus, *J. Power Sources*, 2010, **195**, 939.

Published on 06 Ximoli 2013. Downloaded on 06/02/2026 5:32:02 AM.

6 A. Kraytsberg and Y. Ein-Eli, *Adv. Energy Mater.*, 2012, **2**, 922.
7 H. J. Bang, V. S. Donepudin and J. Prakash, *Electrochim. Acta*, 2002, **48**, 443.
8 K. Amine, H. Tukamoto, H. Yasuda and Y. Fujita, *J. Power Sources*, 1997, **68**, 604.
9 Y. Gao, K. Myrtle, M. J. Zhang, J. N. Reimers and J. R. Dahn, *Phys. Rev. B: Condens. Matter Mater. Phys.*, 1996, **54**, 16670.
10 S. H. Park and Y. K. Sun, *Electrochim. Acta*, 2004, **50**, 439.
11 R. Santhanam and B. Rambabu, *J. Power Sources*, 2010, **195**, 5442.
12 G. Q. Liu, L. Wen and Y. M. Liu, *J. Solid State Electrochem.*, 2010, **14**, 2191.
13 B. L. Ellis, K. T. Lee and L. F. Nazar, *Chem. Mater.*, 2010, **22**, 691.
14 K. Takahashi, M. Saitoh, M. Sano, M. Fujita and K. Kifune, *J. Electrochem. Soc.*, 2004, **151**, A173.
15 Y. Terada, K. Yasaka, F. Nishikawa, T. Konishi, M. Yoshio and I. Nakai, *J. Solid State Chem.*, 2001, **156**, 286.
16 A. Manthiram, *J. Phys. Chem. Lett.*, 2011, **2**, 176.
17 G. Blasse, *J. Phys. Chem. Solids*, 1966, **27**, 383.
18 D. Gryffroy and R. E. Vaudenberghe, *J. Phys. Chem. Solids*, 1992, **53**, 777.
19 N. Amdouni, K. Zaghib, F. Gendron, A. Mauger and C. M. Julien, *J. Magn. Magn. Mater.*, 2007, **309**, 100.
20 J. H. Kim, S. T. Myung, C. S. Yoon, S. G. Kang and Y. K. Sun, *Chem. Mater.*, 2004, **16**, 906.
21 B. J. Hwang, Y. W. Wu, M. Venkateswarlu, M. Y. Cheng and R. Santhanam, *J. Power Sources*, 2009, **193**, 828.
22 J. Liu and A. Manthiram, *J. Phys. Chem. C*, 2009, **113**, 15073.
23 K. J. Hong and Y. K. Sun, *J. Power Sources*, 2002, **109**, 427.
24 Q. Zhong, A. Bonakdarpour, M. Zhang, Y. Gao and J. R. Dahn, *J. Electrochem. Soc.*, 1997, **144**, 205.
25 J. Song, D. W. Shin, Y. Lu, C. D. Amos, A. Manthiram and J. B. Goodenough, *Chem. Mater.*, 2012, **24**, 3101.
26 K. Ariyoshi, Y. Iwakoshi, N. Nakayama and T. Ohzuku, *J. Electrochem. Soc.*, 2004, **151**, A296.
27 Y. Idemoto, H. Narai and N. Koura, *J. Power Sources*, 2003, **119–121**, 125.
28 T. Ohzuku, K. Ariyoshi and S. Yamamoto, *J. Ceram. Soc. Jpn.*, 2002, **110**, 501.
29 J. Zheng, J. Xiao, X. Yu, L. Kovarik, M. Gu, F. Omenya, X. Chen, X. Q. Yang, J. Liu, G. L. Graff, M. S. Whittingham and J. G. Zang, *Phys. Chem. Chem. Phys.*, 2012, **14**, 13515.
30 K. Mukai and J. Sugiyama, *J. Electrochem. Soc.*, 2010, **157**, A672.
31 S. Patoux, L. Daniel, C. Bourbon, H. Lignier, C. Pagano, F. Le Cras, S. Jouanneau and S. Martinet, *J. Power Sources*, 2009, **189**, 344.
32 H. S. Fang, Z. X. Wang, X. H. Li, H. J. Guo and W. J. Peng, *J. Power Sources*, 2006, **153**, 174.
33 Z. Y. Chen, S. Ji, V. Linkov, J. L. Zhang and W. Zhu, *J. Power Sources*, 2009, **189**, 507.
34 H. S. Fang, Z. X. Wang, X. H. Li, Z. L. Yin, H. J. Guo and W. J. Peng, *Chin. J. Inorg. Chem.*, 2006, **22**, 311.
35 X. Y. Feng, C. Shen, X. Fang and C. H. Chen, *Chin. Sci. Bull.*, 2012, **57**, 4176.
36 G. Liu, L. Qi and L. Wen, *Rare Met. Mater. Eng.*, 2006, **35**, 299.
37 H. S. Fang, Z. X. Wang, Z. L. Yin, X. H. Li, H. J. Guo and W. J. Peng, *Trans. Nonferrous Met. Soc. China*, 2005, **15**, 1429.
38 N. Amdouni, K. Zaghib, F. Gendron, A. Mauger and C. M. Julien, *Ionics*, 2006, **12**, 117.
39 Z. Q. Zhao, J. F. Ma, H. Tian, L. J. Xie, J. Zhou, P. W. Wu, Y. G. Wang, J. T. Tao and X. Y. Zhu, *J. Am. Ceram. Soc.*, 2005, **88**, 3549.
40 Y. K. Fan, J. M. Wang, X. B. Ye and J. Q. Zhang, *Mater. Chem. Phys.*, 2007, **103**, 19–23.
41 T. F. Yi and Y. R. Zhu, *Electrochim. Acta*, 2008, **53**, 3120.
42 C. Miao, L. Shi, G. Chen and D. Dai, *Adv. Mater. Res.*, 2012, **463–464**, 881.
43 S. T. Myung, S. Komaba, N. Kumagai, H. Yashiro, H. T. Chung and T. H. Cho, *Electrochim. Acta*, 2002, **47**, 2543.
44 Q. Zhao, N. Ye, L. Li and F. Yan, *Rare Met. Mater. Eng.*, 2010, **39**, 1715.
45 H. Liu, Y. P. Wu, E. Rahm, R. Holze and H. Q. Wu, *J. Solid State Electrochem.*, 2004, **8**, 450.
46 J. H. Choy, D. H. Kim, C. W. Kwon, S. J. Hwang and Y. I. Kim, *J. Power Sources*, 1999, **77**, 1.
47 Y. S. Lee, Y. K. Sun and K. S. Nahm, *Solid State Ionics*, 1998, **109**, 285.
48 J. C. Arrebola, A. Caballero, L. Hernan and J. Morales, *J. Power Sources*, 2008, **180**, 852.
49 A. Cao and A. Manthiram, *ECS Symp. Abstr*, 2012, vol. 2, p. 699.
50 Z. Q. He, L. Z. Xiong, X. M. Wu, W. P. Liu, S. Chen and K. L. Huang, *Chin. J. Inorg. Chem.*, 2007, **23**, 875.
51 Y. Idemoto, H. Sekine, K. Ui and N. Koura, *Electrochemistry*, 2004, **72**, 564.
52 J. Cabana, H. Zheng, A. K. Shukla, C. Kim, V. S. Battaglia and M. Kunduraci, *J. Electrochem. Soc.*, 2011, **158**, A997.
53 M. Kunduraci and G. G. Amatucci, *J. Electrochem. Soc.*, 2006, **153**, A1345.
54 D. Liu, J. Han and J. B. Goodenough, *J. Power Sources*, 2010, **195**, 2918.
55 M. Yamada, B. Dongying, T. Kodera, K. Myoujin and T. Ogihara, *J. Ceram. Soc. Jpn.*, 2009, **117**, 1017.
56 H. M. Wu, J. P. Tu, X. T. Chen, D. Q. Shi, X. B. Zhao and G. S. Cao, *Electrochim. Acta*, 2006, **51**, 4148.
57 Y. K. Sun, G. S. Park, Y. S. Lee, M. Yoshio and K. S. Nahm, *J. Electrochem. Soc.*, 2001, **148**, A994.
58 S. H. Park, S. W. Oh, S. T. Myung, Y. C. Kang and Y. K. Sun, *Solid State Ionics*, 2005, **176**, 481.
59 T. Ogihara, T. Kodera, K. Myoujin and S. Motohira, *Mater. Sci. Eng., B*, 2009, **161**, 109.
60 T. A. Arunkumar and A. Manthiram, *Electrochim. Acta*, 2005, **50**, 5568.
61 G. B. Zhong, Y. Y. Wang, Y. Q. Yu and C. H. Chen, *J. Power Sources*, 2012, **205**, 385.
62 D. Liu, Y. Lu and J. B. Goodenough, *J. Electrochem. Soc.*, 2010, **157**, A1269.
63 D. W. Shin and A. Manthiram, *Electrochem. Commun.*, 2011, **13**, 1213.
64 D. Liu, J. Hamel-Paquet, J. Trottier, F. Barray, V. Gariépy, P. Hovington, A. Guerfi, A. Mauger, C. M. Julien,

 This journal is © The Royal Society of Chemistry 2014

Published on 06 Ximoli 2013. Downloaded on 06/02/2026 5:32:02 AM.

J. B. Goodenough and K. Zaghib, *J. Power Sources*, 2012, **217**, 400.
65 M. Kunduraci, J. F. Al-Sharab and G. G. Amatucci, *Chem. Mater.*, 2006, **18**, 3585.
66 X. Ma, B. Kang and G. Ceder, *J. Electrochem. Soc.*, 2010, **157**, A925.
67 J. H. Kim, C. S. Yoon, S. T. Myung, J. Prakash and Y. K. Sun, *Electrochem. Solid-State Lett.*, 2004, **7**, A216.
68 M. Kunduraci and G. G. Amatucci, *J. Power Sources*, 2007, **165**, 359.
69 P. Strobel, A. Ibarra-Palos, M. Anne and F. Le Cras, *J. Mater. Chem.*, 2000, **10**, 429.
70 T. Nakamura, Y. Yamada and M. Tabuchi, *J. Appl. Phys.*, 2005, **98**, 93905.
71 J. B. Goodenough, *Magnetism and the Chemical Bond*, Wiley, New York, 1963.
72 F. G. B. Ooms, E. M. Kelder, J. Schoonman, M. Wagemaker and F. M. Mulder, *Solid State Ionics*, 2002, **152**, 143.
73 D. W. Shin and A. Manthiram, *Electrochem. Commun.*, 2011, **13**, 121.
74 L. Wang, H. Li, X. Huang and E. Baudrin, *Solid State Ionics*, 2011, **193**, 32.
75 K. Rhodes, R. Meisner, Y. Kim, N. Dudney and C. Daniel, *J. Electrochem. Soc.*, 2011, **158**, A890.
76 B. Hai, A. K. Shukla, H. Duncan and G. Chen, *J. Mater. Chem. A*, 2013, **1**, 759.
77 W. Zhu, D. Liu, J. Trottier, C. Gagnon, A. Mauger, C. M. Julien and K. Zaghib, *J. Power Sources*, 2013, **242**, 236–243.
78 R. A. Huggins, *J. Electrochem. Soc.*, 2013, **160**, 3001.
79 J. Liu and A. Manthiram, *Chem. Mater.*, 2009, **21**, 1695.
80 Y. K. Sun, K.-J. Hong, J. Prakash and K. Amine, *Electrochem. Commun.*, 2002, **4**, 344.
81 T. Noguchi, I. Yamazaki, T. Numata and M. Shirakata, *J. Power Sources*, 2007, **174**, 359.
82 Y. K. Sun, Y. S. Lee, M. Yoshio and K. Amine, *Electrochem. Solid-State Lett.*, 2002, **5**, 99.
83 Y. Kobayashi, H. Miyashiro, K. Takei, H. Shigemura, M. Tabuchi, H. Kageyama and T. Iwahori, *J. Electrochem. Soc.*, 2003, **150**, 1577.
84 J. Y. Shi, C.-W. Yi and K. Kim, *J. Power Sources*, 2010, **195**, 6860.
85 H. M. Wu, I. Belharouak, A. Abouimrane, Y.-K. Sun and K. Amine, *J. Power Sources*, 2010, **195**, 2909.
86 D. Liu, J. Trottier, P. Charest, J. Fréchette, A. Guerfi, A. Mauger, C. M. Julien and K. Zaghib, *J. Power Sources*, 2012, **204**, 127.
87 C. Zhu, Y. Yu, L. Gu, K. Weichert and J. Maier, *Angew. Chem., Int. Ed.*, 2011, **50**, 6278.
88 K. Zaghib, N. Ravet, M. Gauthier, F. Gendron, A. Mauger, J. B. Goodenough and C. M. Julien, *J. Power Sources*, 2006, **163**, 560.